$O(^3P_J)$ Alignment from the Photodissociation of SO_2 at 193 nm†

M. Brouard,* R. Cireasa,‡ A. P. Clark, T. J. Preston, and C. Vallance

The Department of Chemistry, University of Oxford, The Physical and Theoretical Chemistry Laboratory, South Parks Road, Oxford, OX1 3QZ, United Kingdom

G. C. Groenenboom

Institute of Theoretical Chemistry, NSRIM, University of Nijmegen, Toernooiveld 1, 6525 ED Nijmegen, The Netherlands

O. S. Vasyutinskii

Ioffe Institute, Russian Academy of Sciences, 194021 St. Petersburg, Russia

Received: February 14, 2004; In Final Form: March 16, 2004

The 193-nm photodissociation of SO_2 has been studied using the resonantly enhanced multiphoton ionization of ground-state $O(^3P_J)$, coupled with velocity-map ion imaging. The dependence of the ion images on the linear polarization of pump and probe radiation has been used to determine the electronic angular momentum alignment of the recoiling, state-selected atoms, together with their speed distribution and translational anisotropy. The polarization data for $J = 1$ and 2 have been used to estimate the state multipole moments of the O-atom electron spin and orbital angular momenta. The data suggest that both sources of O-atom electronic angular momentum are polarized. It is shown that the spin polarization could either arise from exit-channel couplings or be a manifestation of the participation of triplet states in the dissociation. The angular dependence of the potential energy in the exit channel is examined using long-range quadrupole−dipole and quadrupole−quadrupole interaction terms, from which molecular-frame multipole moments of the orbital angular momentum of the recoiling O atoms have been calculated. Comparison with the experimentally derived multipole moments is used to help provide insight into the dissociation mechanism. The results are also discussed in light of similar experimental data from the photodissociation of N_2O.

1. Introduction

The spectroscopic properties and photodissociation dynamics of sulfur dioxide, an important trace species in the atmosphere, have been subjected to many studies over the past three decades. The $\tilde{C}^1B_2 \leftarrow \tilde{X}^1A_1$ electronic transition is known to begin at around 240 nm,[1] with predissociation into $O(^3P) + SO(^3\Sigma^-)$ products occurring above a threshold at approximately 219 nm.[1−5] Dynamical measurements have been conducted, using a range of experimental techniques, over a wavelength range of 193−218 nm, where the excess energy is insufficient to permit the formation of electronically excited products. However, despite this apparently simplifying constraint, the details of the dissociation mechanism are yet to be explained unambiguously.

A preliminary understanding of the subtleties at play in this system may be gained with reference to the schematic diagram of some of the low-lying electronic states of SO_2 provided in Figure 1.[6] At linearity, the approach from the separated $O(^3P)$ and $SO(^3\Sigma^-)$ fragments yields surfaces of $^1\Sigma^+$, $^1\Pi$, $^3\Sigma^+$, and $^3\Pi$ symmetries (along with $^5\Sigma^+$ and $^5\Pi$ surfaces that are generally assumed to play no part in the dissociation process). On bending, these states correlate with those in the C_s configuration that describes the dissociative pathway in the following manner:[6]

(1) The $^1\Sigma^+$ surface correlates with the ground $1^1A'$ molecular state.

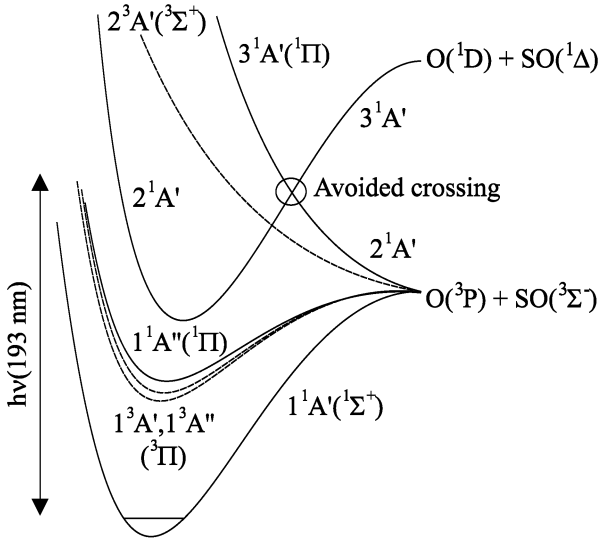

Figure 1. Schematic diagram of the relevant potential curves adapted from Katagiri et al.[6] In parentheses are the symmetries of the states at linearity in the long-range region. The electronic state accessed at 193 nm is the $\tilde{C}^1B_2(2^1A')$ state.

† Part of the special issue "Richard Bersohn Memorial Issue".

* Corresponding author. E-mail: mark.brouard@chemistry.ox.ac.uk.

‡ Permanent address: Laser Department, National Institute of Laser, Plasma and Radiation Physics, P.O. Box MG-36, Bucharest, Romania.

10.1021/jp049328v CCC: $27.50
Published on Web 05/07/2004

(2) The $^1\Pi$ surface splits into a stabilized $1^1A''$ state and, at long range, the repulsive $2^1A'$ state.

(3) The $^3\Sigma^+$ surface correlates with the repulsive $2^3A'$ state.

(4) The $^3\Pi$ surface splits into the stabilized $1^3A'$ and $1^3A''$ states.

Excitation in the wavelength range of 193−218 nm accesses the $2^1A'$ surface (the $\tilde{C}^1B_2$ state in C_{2v} symmetry), which correlates with electronically excited (and energetically inaccessible) $SO(^1\Delta) + O(^1D)$ products.[6] It has been suggested that dissociation to the observed products may occur through one, or more, of the following mechanistic pathways:

(1) an internal conversion mechanism to quasi-bound continuum levels of the $1^1A'$ground state;[3,6,7]

(2) an intersystem crossing onto the repulsive $2^3A'$ surface;[4,8]

(3) an avoided crossing with the $3^1A'$ state.[9,10]

In 2000, Houston and co-workers provided a comprehensive summary of the experimental and theoretical studies concerning the SO_2 predissociation process that had been published up until that time.[11] The review emphasized the extent of the interpretive disagreement in the literature, with arguments being raised variously for the internal conversion,[3,6,7] the intersystem crossing,[4,8] and the avoided crossing mechanisms[9,10] being the dominant dissociative pathways over a variety of excitation energies. The authors subsequently conducted an ion-imaging study of the photolysis at selected wavelengths between 202 and 207 nm.[11] They argued that the variations in the vibrational-energy partitioning in the SO fragments, inferred through the velocity distributions of the detected $O(^3P)$ atoms were consistent with a wavelength-dependent dissociation mechanism. The velocity distribution at wavelengths above 203 nm, which was found to be characterized by a relatively uniform partitioning among the energetically accessible levels, was attributed to a dissociation via an internal conversion mechanism to very high vibrational levels of the molecular ground state. Conversely, the images recorded at shorter wavelengths appeared to give rise to SO fragments formed predominantly in their ground vibrational state, an observation ascribed to dissociation via crossing onto the singlet repulsive state. Although a number of experiments conducted near the dissociation threshold have indeed concluded that in this region an internal conversion is the most likely dissociation pathway,[3,6,7] certain other recent evidence has also pointed toward a change in the reaction mechanism at longer wavelengths. In particular, Ray et al.,[10] studying dispersed emission spectra at excitation energies around 200 nm, suggested that the observation of nominally forbidden transitions involving odd quanta in the SO_2 ν_3 band could be explained by a curve crossing of the repulsive $3^1A'$ state with the $\tilde{C}^1B_2(2^1A')$ surface. Ab initio calculations performed by Bludsky et al. on the vibrational states of SO_2 in the $\tilde{C}^1B_2$ state[12] supported these conclusions, although the same authors did point out in a later paper[13] that the strong activity in the emissions seen in these experiments was not necessarily indicative of mixing to the repulsive singlet state.

Nonetheless, close inspection of the literature raises several issues that are yet to be explained in a unified picture of the predissociation process. For example, in a number of earlier experimental measurements[14−16] conducted at 193 nm, the vibrational-state distribution of the nascent $SO(^3\Sigma^-)$ products was found to be strongly inverted and to peak in $v = 2$ (rather than in $v = 0$). Although SO vibrational populations distributions between 193 and 202 nm might help to shed light on the reason for the differences in behavior observed at short and long wavelengths, unfortunately these are not currently available. On the basis of their experimental and theoretical study, Katagiri and co-workers[6] concluded that the internal-conversion mechanism was dominant over the entire wavelength range of 200−220 nm, although their theoretical calculations did allow the possibility of some minor contributions to the dissociation from crossings onto either the $2^3A'$ or $3^1A'$ surfaces. A recent Fourier transform infrared study of the photolysis at 193 nm conducted by Weiner and co-workers[17] led the authors to suggest that, even in this high-excess-energy domain, the dissociation did indeed occur predominantly via internal conversion to the ground state.

One aspect of the dissociation process that may help to disentangle these ambiguities further lies in the possibility of measuring the angular momentum polarization of the observed products. Angular momentum alignment was indeed identified, qualitatively, in the oxygen atoms detected in the ion-imaging experiments by Houston and co-workers. Recent theoretical advances[18] have introduced the possibility of quantifying the alignment of $O(^3P)$ products arising from such systems. Such an approach has been demonstrated in a recent study of N_2O photolysis conducted within this group.[21] Because the presence of angular momentum alignment in an atomic product relates directly to the polarization of either or both of the orbital and spin angular momenta of the unpaired electrons in the atom, it provides a particularly sensitive measure of the evolving molecular structure. For example, by invoking a "fast-dissociation model" in ref 21 in which the electron spin was assumed to be unpolarized, it was possible to use these measurements to make an assignment of the potential energy surface(s) on which the product wave function must be evolving.

In the work presented here, velocity-map ion imaging has been used to measure the $O(^3P_J)$ photofragment speed distributions, speed-dependent translational anisotropies, and atomic angular momentum alignment parameters for each of the three spin−orbit states ($J = 0, 1, 2$) following photolysis at a wavelength of 193 nm. The former two measurements provide confirmation of a number of previous findings.[14−16,33,37] The new results are presented in section 3, following a brief description of the experimental and data analysis procedures in section 2. In section 4, the data are discussed in light of a model in which the spin−orbit interaction in the recoiling O atom is included explicitly and in light of new theoretical calculations of the angular dependence of the long-range potential energy curves. Finally, our principal findings are summarized in section 5.

2. Method

2.1. Experimental Procedures. The experiments were carried out using a standard velocity-map ion-imaging apparatus, which has been described in detail previously.[19−21] Briefly, a mixture of 5% SO_2 seeded in He at a backing pressure of 2 bars was expanded through a pulsed nozzle (General valve) with a 0.8-mm-diameter orifice and collimated by a 1-mm-diameter skimmer. The rotational temperature of the beam was determined to be ∼50 K. Further downstream, the molecular beam was passed through a 2-mm hole in the repeller plate of the velocity-mapping ion optics assembly and crossed 5 cm away from the nozzle exit by two counterpropagating laser beams. The photolysis radiation was provided by a Lambda Physik EMG103 excimer laser operating at 193 nm, and the probe radiation was obtained by frequency doubling the output of an excimer-pumped dye laser (Lambda Physik LPD series). The time delay between the two laser pulses was ∼10 ns. Two plano-convex lenses of 30-cm focal length were used to focus the radiation onto the molecular beam. The $O(^3P_J)$ photofragments were probed by (2 + 1) resonantly enhanced multiphoton

ionization (REMPI) via the $3p\ ^3P \leftarrow {}^3P_J$ transitions near 225 nm. The probe laser energy was attenuated to around 500 μJ pulse^{-1} to reduce to an insignificant level the signal arising from the probe laser alone. During image acquisition, the probe-laser wavelength was scanned over the Doppler profile of the $O(^3P)$ transitions to ensure an equal detection sensitivity for all of the product velocities. The oxygen ions were velocity mapped onto an imaging detector consisting of 40-mm chevron double-microchannel plates (MCPs) coupled to a P47 phosphor screen (DelMar Ventures). The image on the phosphor was captured by an intensified charge-coupled device (CCD) camera (Photonic Science), electronically gated to the flight time of the detected ions and sent to a PC for signal processing (thresholding, event counting,[32] and accumulation). Images were averaged over 20 000 laser shots. Velocity calibration of the final images was achieved using images of $O(^3P)$ from the photodissociation of O_2, the energetics for which are well characterized.

To extract information on $O(^3P_J)$ alignment, images were obtained in four geometries, labeled HH, HV, VH, and VV, according to the polarization of the pump and probe lasers lying parallel (H) or perpendicular (V) to the image plane. These geometries are equivalent to Cases I to IV in the notation used by Dixon.[25] Pairs of images were collected simultaneously using a photoelastic modulator to switch the polarization of the probe laser every shot. This procedure not only reduced the errors due to experimental drift during the measurements but also enabled the measurement of the total angular momentum alignment, $\langle A_{20}\rangle$, from the measured intensity ratios. This alignment parameter is required to normalize the image intensity prior to data analysis.

Separate REMPI spectra were recorded to determine the relative spin−orbit populations arising from the photolysis. For this purpose, the total signal output of the phosphor screen was sent to a boxcar averager, gated at the appropriate arrival time. The integrated signal corresponding to each spin−orbit state was used to determine the ratio of the photofragment populations.

2.2. Data Analysis. The method used to extract dynamical information from the velocity-map images is identical to that described in a previous paper on N_2O photolysis.[21] Briefly, the laboratory (lab) frame scattering distribution $P(v, \Omega_v, \Omega_j)$ of the $O(^3P)$ product following the polarized laser photolysis of SO_2 may be expanded semiclassically in spherical harmonics:

$$P(v, \Omega_v, \Omega_j) = \sum_{k,q} \rho_q^k(v,\Omega_v)\, C_{kq}^*(\Omega_j) \qquad (1)$$

v is the product speed, and $\Omega_v = (\theta_v,\phi_v)$ and $\Omega_j = (\theta_j,\phi_j)$ are the lab frame polar coordinates of the product velocity vector (i.e., the scattering angle) and total angular momentum vector, respectively. The expansion coefficients (or rotational moments) $\rho_q^k(v, \Omega_v)$ are functions of both velocity and scattering angle, and the spherical harmonics depend only on the angular momentum polar coordinates Ω_j. The lab frame is defined such that the z axis lies along the polarization vector and the x axis lies along the propagation vector of the photolysis light. The first step in obtaining the rotational moments of a velocity-map image is to express the distribution in eq 1 in terms of coordinates in a new reference frame, known as the time-of-flight (TOF) frame, in which z lies along the time-of-flight axis. (x is still defined to lie along the photolysis laser propagation direction.) The image rotational moments are then obtained simply by integrating the distribution along the time-of-flight axis, mirroring the compression of the ion cloud along this axis during the experiment. A second rotation, to a detection frame, is often required to allow the use of expressions in the literature for the rotational line strengths. (See, for example, ref 31.) The final expression for the rotational moments of the images may then be written as

$$\rho_{q''}^k(v_p, \phi_T)_{DET} = \frac{1}{4\pi}\sum_{q'} e^{iq'\phi_T} \sum_{K=0,2} \sum_{k_1} [1 + (-1)^{k_1+q'}] \times f_0^K(k_1, k, q', q'', R, R')\, F_0^K(k_1, k, q'; v_p) \qquad (2)$$

in which v_p and ϕ_T are the radial and angular coordinates of the image, respectively, and θ_T is the angle that the product velocity vector makes with the time-of-flight axis. $R = (\alpha, \beta, \gamma)$ and $R' = (\alpha', \beta', \gamma')$ are Euler angles for the frame transformations, defined in Table 1 of ref 19. The indices k_1, q' and k, q'' denote the spherical harmonic components of the velocity and angular momentum distributions of the product in the final or "detection" reference frame.

Equation 2 takes the form of a Fourier cosine series in which the coefficient of each term is a sum over products of "geometrical factors" f_0^K and "dynamical factors" F_0^K. The geometrical factors depend only on the experimental geometry and are easily calculated, but the dynamical factors are functions of a set of alignment parameters that define the scattering dynamics. Analytical expressions for the f_0^K and F_0^K factors have been given in previous publications.[19−21] Note that simple relationships exist between each of the commonly used sets of alignment parameters (e.g., the bipolar moments $b_0^K(k_1, k; v)$ introduced in the semiclassical treatment by Dixon,[25] the polarization parameters $a_q^k(p)$ used by Rakitzis et al.,[28,29] and the alignment anisotropy parameters of Vasyutinskii and coworkers[27]). Here we use the alignment anisotropy parameters β_2, s_2, α_2, γ_2, and η_2 because these are appropriate for a full quantum-mechanical treatment of photodissociation.[27]

The Hertel−Stoll scheme[26] is used to convert the (potentially) complex quantities $\rho_{q''}^k$ into the real quantities $\rho_{q''\pm}^k$:

$$\rho_{q''+}^k(v_p, \phi_T) = \frac{1}{\sqrt{2}}[(-1)^{q''}\rho_{+q''}^k(v_p, \phi_T) + \rho_{-q''}^k(v_p, \phi_T)] \qquad 1 \le q'' \le k \qquad (3)$$

and

$$\rho_{0+}^k(v_p, \phi_T) = \rho_0^k(v_p, \phi_T) \qquad (4)$$

Using linearly polarized pump and probe radiation and probing the $O(^3P)$ photofragments via (2 + 1) REMPI, we find that the analytical form of the images obtained depends only on the ρ_0^0, ρ_0^2, and ρ_{2+}^2 rotational moments. For the four experimental

TABLE 1: Vibrational Populations of the SO Photofragments of the 193-nm Photodissociation of SO_2 as Estimated by the Simulation of the Observed $O(^3P_J)$ Speed Distributions Shown in Figure 4[a]

level	population
$v' = 0$	0.09(1)
$v' = 1$	0.23(2)
$v' = 2$	0.56(5)
$v' = 3$	0.06(2)
$v' = 4$	0.06(2)
$v' = 5$	–

[a] Data have been averaged over O-atom spin−orbit state J. Errors in the last decimal place are given in parentheses.

geometries used, the appropriate expressions for the images are[20,27]

$$\mathscr{I}_{HV}(v_p, \phi_T) = \mathscr{I}_{VV}(v_p, \phi_T) = \rho_0^0(v_p, \phi_T) + \sqrt{5}\frac{P_2}{P_0}\rho_0^2(v_p, \phi_T)$$

$$\mathscr{I}_{VH}(v_p, \phi_T) = \mathscr{I}_{HH}(v_p, \phi_T) = \rho_0^0(v_p, \phi_T) - \frac{\sqrt{5}}{2}\frac{P_2}{P_0}[\rho_0^2(v_p, \phi_T) + \sqrt{3}\rho_{2+}^2(v_p, \phi_T)] \quad (5)$$

where P_2/P_0 is the line-strength factor for the probe (2 + 1) REMPI transition, taking the values 0, $\sqrt{1/2}$, and $-\sqrt{7/10}$ for the $J = 0$, 1, and 2 spin−orbit components of O(^{3}P).[18,30] Explicit expressions for the $\rho_q^k(v_p, \phi_T)$ appearing in these equations have been given by Bracker et al.[27]

These expressions may be used in conjunction with eqs 2 and 3 to obtain analytical expressions for the Fourier moments of the measured images. As described previously,[21] here we have used a basis set made up of a sum of Gaussian functions to describe the speed dependence of the various angular momentum polarization parameters. These may be fit to the Fourier moments extracted from the experimental data in order to obtain the (velocity-dependent) alignment parameters characterizing the scattering distribution using the methodology described in ref 21. The experimental Fourier moments, $c_n(v_p)$, of the ion images, $\mathscr{I}(v_x,v_y)v_p = \mathscr{I}(v_p,\phi_T)$, are defined as

$$c_n(v_p) = N\int_0^{2\pi}\mathscr{I}(v_x, v_y)\cos(n\phi_T)v_p\, d\phi_T \quad (6)$$

where the normalization constant N is equal to 1 when $n = 0$ and $N = 2$ when $n > 0$. With linearly polarized pump and probe radiation, n is restricted to even terms.

Four sets of images were collected for each experimental geometry and spin−orbit state of O(^{3}P) and used to determine the alignment parameters. Error estimates for the alignment parameters are given as the standard deviation in the parameters returned from fits to the individual sets of data, unless otherwise stated.

3. Results

3.1. Spin−Orbit State Populations. O-atom spin−orbit populations were obtained directly from the integrated REMPI transition intensities, as described in section 2.1. The resulting relative values for J = 0:1:2 were 1:2.3(2):4.6(4), which are very close to the statistical ratio of the spin−orbit state degeneracies 1:3:5 (further discussion in section 4.1). The measured population ratios are in reasonable agreement with those of Abe et al.,[33] 1:2.5:7.6, and those of Huang and Gordon,[34] 1:2.6:5.2, both obtained using VUV laser-induced fluorescence and a photolysis wavelength of 193 nm. Houston and co-workers[11] also determined spin−orbit population ratios in the wavelength region from 202−207 nm using velocity-map ion imaging. Their values vary quite markedly with photolysis wavelength and kinetic energy release, but those measured at 202.13 nm (1:2.2:3.2), at which wavelength the kinetic energy release is quite similar to that in the present measurements, are reasonably close to the values obtained here at 193 nm. By contrast, the elegant state-to-state experiments of Tiemann and co-workers[5,35,36] close to the dissociation threshold reveal a much stronger preference for population of the O(^{3}P$_2$) ground state, consistent with near-adiabatic dissociation at low product recoil energies.

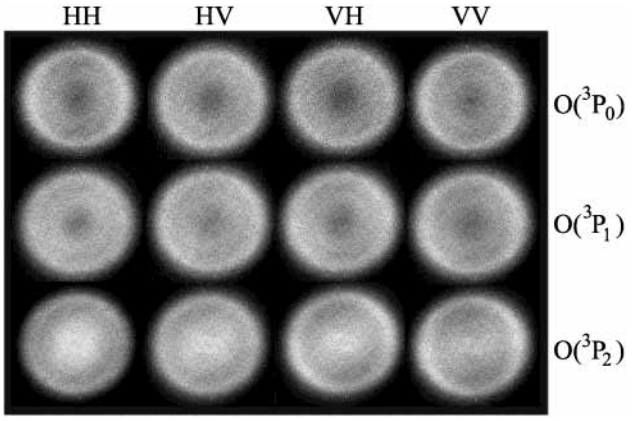

Figure 2. Velocity-map ion images of the O(^{3}P$_J$) $J = 0$ (top row), 1 (middle row), and 2 (bottom row) fragments generated by 193-nm photodissociation of SO_2. The four columns show images obtained in the HH, HV, VH, and VV pump−probe geometries, as described in the text.

3.2. O(^{3}P) Speed Distribution and SO($^3\Sigma^-$) Internal State Populations. The complete set of velocity-map ion images is shown in Figure 2, and the first three even Fourier moments of these images, together with the fits to them using the procedures described in section 2, are shown in Figure 3. The analysis first yields the speed distribution of the quantum state-selected O(^{3}P$_J$) photofragments. The three speed distributions are compared in Figure 4. The fact that they are so similar supports the view that the spin−orbit states have a common dynamical origin, with the population of the three states determined in the exit channel. Both the Fourier moments of the images and the resulting speed distributions show some structure, which is probably associated with the population of vibrational levels in the SO(X) cofragment. Similar structure has been observed previously at 193 nm in the TOF experiments of Kawasaki and Sato[16] and Huber and co-workers[15,37] and in the wavelength range of 202−207 nm by Houston and co-workers.[11]

To estimate the SO vibrational populations, we fit the speed distributions shown in Figure 4 with a sum of Gaussian functions, each corresponding to the SO cofragment born in a different vibrational state. The widths of the Gaussians, together with the vibrational populations for levels $v' = 0-5$, were used as adjustable parameters in the fit. The Gaussians widths returned from the analysis and their precise location on the velocity scale provide some indication of the mean rotational energy of the SO fragments. We obtain a mean rotational excitation of ~700 cm^{-1}, in reasonable accord with the data of Huber and co-workers.[37] Judging from the widths of the structures seen in the longer-wavelength study of Houston and co-workers,[11] the degrees of rotational excitation observed in the short- and long-wavelength studies must be quite similar.

The vibrational populations derived from the fits, again averaged over the O-atom spin−orbit state, are shown in Table 1. The data are very similar to those obtained previously at 193 nm.[8,14−16,39] All studies agree that the most populated SO photofragment vibrational level is $v = 2$, although there is some disagreement about the extent of the population of neighboring vibrational levels,[8,14−16,39] probably arising from differences in energy resolution. In contrast to the rotational excitation, note that the vibrational distribution at 193 nm is found to be quite different from those obtained by Houston and co-workers[11] in the range of 202−207 nm.

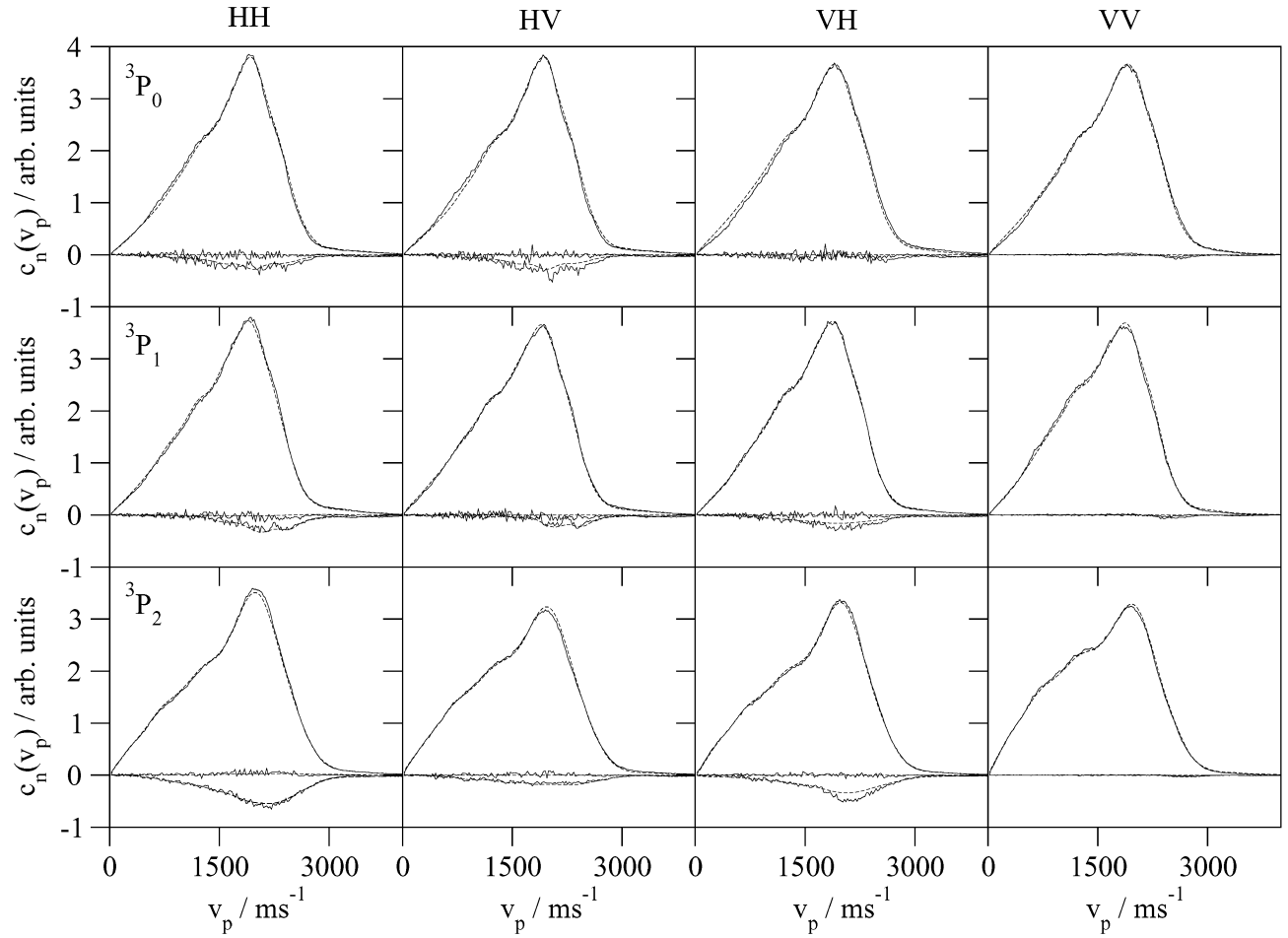

Figure 3. Same as for Figure 2 but showing the first three even Fourier moments, $c_{0,2,4}(v_p)$, of the raw ion images, together with the fits to the data (dotted lines) using the procedures described in section 2.2. Note that the $c_4(v_p)$ moments are almost zero for all of the images shown in Figure 2 and that the $c_2(v_p)$ moments are either zero on symmetry grounds or are slightly negative.

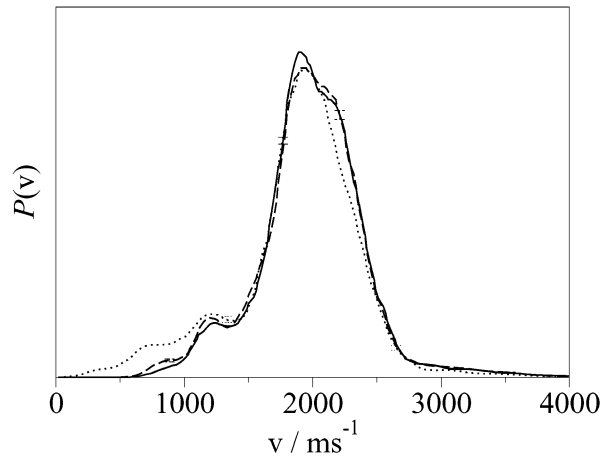

Figure 4. Comparison of the speed distributions, $P(v)$, obtained for the three O(^3P_J) spin−orbit states. After the transformation to kinetic energy release, fits to the data yielded the vibrational populations shown in Table 1, as described in the text. The lines are coded as follows: — $^3P_0$, − − − $^3P_1$, and ··· $^3P_2$. The error bars represent 2σ.

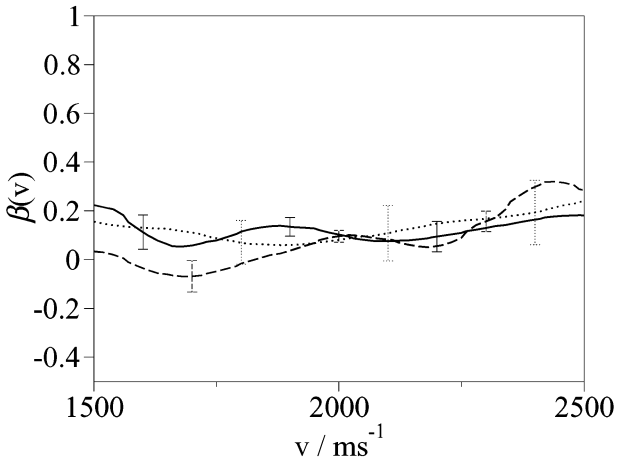

Figure 5. Same as for Figure 4 but showing the speed-dependent translational anisotropies, $\beta(v)$, for the three probed O-atom spin−orbit states. Notice that the *y*-axis scale has been expanded to half the full range of the translational anisotropy. The three lines refer to the three spin−orbit states of oxygen and are labeled as in Figure 4. The error bars represent 2σ.

3.3. Angular Distributions. The speed-dependent translational anisotropies, $\beta(v)$, returned from the Fourier moment analysis are shown in Figure 5 for the three O(^3P_J) spin−orbit states. The present experiments reveal a small but measurable anisotropy parameter with no obvious systematic trend with O-atom speed (or, equivalently, with SO internal quantum state). The speed-averaged values for the three O-atom spin−orbit states are given in Table 2. The mean of these, $\beta \approx 0.12$, may be interpreted as arising from the slow predissociation of a prolate top molecule, which closely describes the inertial character of SO_2. The important quantity in determining β in this limit is the dissociation lifetime τ relative to the rotational period ω, characterized by the parameter $\tau^* = \omega\tau$.[38] The lifetime

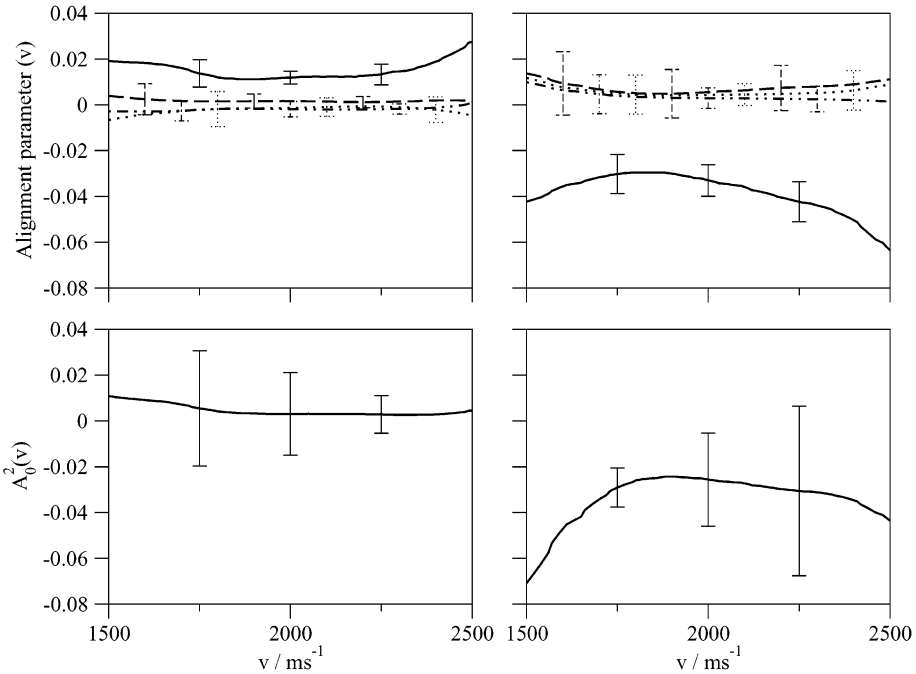

Figure 6. Speed dependence of the alignment anisotropy parameters (upper panels) and the total alignment (lower panels), $A_{20}(v) = -2(\alpha_2 + \gamma_2 + \eta_2)$, for O(^{3}P) atoms born in $J = 1$ (left panels) and $J = 2$ (right panels). The full ranges of the alignment parameters is given in ref 21. In the upper panels, alignment anisotropy parameters are coded as follows: — s_2, − − − α_2, − ·· − ·· γ_2, and ··· η_2. The error bars represent 2σ.

TABLE 2: Velocity-Averaged Spatial Anisotropy and Alignment Anisotropy Parameters for the O(^{3}P) Products of 193-nm SO_2 Photolysis[a]

	O(^{3}P$_0$)	O(^{3}P$_1$)	O(^{3}P$_2$)
β	+0.15(2)	+0.07(2)	+0.13(2)
s_2		+0.018(3)	−0.040(4)
α_2		+0.003(2)	+0.009(3)
γ_2		−0.001(1)	+0.003(2)
η_2		−0.005(2)	+0.008(5)
$\langle A^2_0\rangle^b$		+0.005(1)	−0.040(2)
$\langle A^2_0\rangle^c$		+0.005	−0.035

[a] Alignment parameters are given to three decimal places, with error estimates in the final decimal place given in parentheses. [b] Determined from the fitting procedure. [c] Determined from the relative total intensities of images collected in different experimental geometries.

of SO_2(C) after excitation at 193 nm is known to be $\tau \approx 25$ ps,[6] and an estimate of the rotational angular frequency, ω, may be obtained using the classical expression

$$E_{\mathrm{rot}} = \frac{1}{2} I\omega^2$$

assuming a parent molecular rotational temperature of ~50 K. The resulting value of τ^* is found to be ~30, which is sufficiently large to be able to assume that the parent molecule survives for many rotational periods prior to dissociation. Bersohn and co-workers have shown that under these conditions β may be written as[38]

$$\beta = \langle\langle D^{(2)}_{00}(\delta\Omega(\infty))\rangle\rangle\beta_0 \approx 0.17\beta_0$$

The expectation value $\langle\langle D^{(2)}_{00}(\delta\Omega(\infty))\rangle\rangle$ has been evaluated using the data from Table 2 of ref 38. β_0 represents the value of β in the prompt recoil limit. Assuming that the transition moment for the SO_2 transition lies along an axis parallel to the two oxygen atoms (as it should for the C ← X transition) and that SO_2 possesses an excited-state bond angle of ~104°,[46] β_0 can be estimated to be ~0.4. This would yield $\beta \approx 0.17\beta_0 = 0.07$, in qualitative agreement with the measured value of 0.12.

Previous measurements of the translational anisotropy of SO_2 photodissociation at 193 nm have yielded values close to zero.[15,39] However, the present value of ~0.1 is within previous experimental error. In their recent velocity-map ion-imaging study of the photodissociation of SO_2 at wavelengths centered around 205 nm, Houston and co-workers also reported a small anisotropy but ascribed this to the effects of angular momentum polarization.[11] In the present work, the availability of the necessary line-strength factors[18] has made it possible to decouple fully the effects of translational anisotropy and rotational polarization.

3.4. Angular Momentum Polarization. An analysis of the probe-laser polarization dependence of the ion images for the O(^{3}P$_1$) and O(^{3}P$_2$) atomic products yields the angular momentum polarization parameters, as described in section 2.2. Images for the O(^{3}P$_0$) photofragments sensibly showed no dependence on probe polarization. The speed dependences of the alignment anisotropy parameters s_2, α_2, γ_2, and η_2 for the two spin−orbit states are shown in the upper panels of Figure 6. The velocity-dependent total alignments $\langle A_{20}\rangle = -2(\alpha_2 + \gamma_2 + \eta_2)$[27] are shown in the lower panels of Figure 6. The total alignment may be determined either from the intensity differences between images obtained in different pump−probe geometries or from separate measurements in which the total REMPI intensity is monitored as a function of probe polarization.[21] The two methods yield essentially the same results (Table 2) and provide a useful check of the self-consistency of the data and its analysis. Note that the magnitude of the alignment for the $J = 1$ fragments is significantly smaller than that for the $J = 2$ fragments, a feature that is also clear from an inspection of the Fourier moments of the images shown in Figure 3.

The most notable feature of the data shown in Figure 6 is that the signs of all of the alignment parameters, apart from α_2, which is subject to relatively large errors, are opposite for the O atoms formed in $J = 1$ and 2. This behavior is similar to that observed in the O(^{3}P$_J$) products of the photodissociation of N_2O.[21] The alignment anisotropy parameters show little systematic behavior with recoil speed, and their speed-averaged

TABLE 3: Molecular Frame Multipole Moments of the Total Electronic Angular Momentum, $\rho_{KQ}(J)$, for $O(^3P_1)$ and $O(^3P_2)$ Products of 193-nm SO_2 Photolysis, Averaged over Scattering Angle[a]

$\rho_{KQ}(J)/\rho_{00}(J)$	$O(^3P_1)$	$O(^3P_2)$
$\rho_{20}(J)/\rho_{00}(J)$	+0.12(3)	−0.26(3)
$\mathcal{R}[\rho_{21}(J)]/\rho_{00}(J)$	+0.003(3)	−0.007(4)
$\rho_{22}(J)/\rho_{00}(J)$	+0.011(3)	−0.016(9)

[a] Errors in the last decimal place are given in parentheses.

values are collected in Table 2. Another notable feature of the alignment anisotropy parameters is that they are dominated by the parameter s_2. This parameter is related to the semiclassical bipolar moment $\beta_0^0(22)$[40] (often referred to as the $v-j$ correlation[25]). In the limit in which all memory of the laboratory frame alignment of the transition moment is lost, the $v-j$ correlation is the only surviving alignment parameter.[41,42] The low value of β observed here suggests that although there is some memory of the initial alignment of the transition moment it will not be possible to determine all of the molecular frame moments of the angular momentum distribution with equal sensitivity.

The alignment anisotropy parameters may be transformed into molecular frame parameters using the equations[21,27]

$$\frac{\rho_{20}(J)}{\rho_{00}(J)} = \sqrt{5}V(J)\frac{[s_2 - 2\alpha_2 P_2(\cos\theta_t)]}{[1 + \beta_0 P_2(\cos\theta_t)]} \quad (7)$$

$$\frac{\mathcal{R}[\rho_{21}(J)]}{\rho_{00}(J)} = -\frac{\sqrt{30}V(J)}{2}\frac{\gamma_2 \sin\theta_t \cos\theta_t}{[1 + \beta_0 P_2(\cos\theta_t)]} \quad (8)$$

$$\frac{\rho_{22}(J)}{\rho_{00}(J)} = -\frac{\sqrt{30}V(J)}{4}\frac{\eta_2 \sin^2\theta_t}{[1 + \beta_0 P_2(\cos\theta_t)]} \quad (9)$$

where $V(1) = \sqrt{10}$ and $V(2) = 5\sqrt{2/7}$. Note that the molecular-frame multipole moments depend in principle on the scattering angle θ_t relative to the electric vector of the photolysis light. However, because s_2 is much larger than the other polarization moments, the scattering-angle dependence of the molecular-frame moments is not significant, and instead here we use the speed-averaged alignment anisotropy parameters from Table 2, together with the above equations, to obtain the scattering-angle-averaged molecular-frame multipole moments $\rho_{2Q}(J)$ shown in Table 3. Consistent with the above discussion concerning the parameter s_2, the molecular multipole moments are dominated by the contribution from $\rho_{20}(J)$, as seen from eq 7. As with the polarization anisotropy parameters, the multipole moments for $J = 1$ and 2 are opposite in sign, just as they are in the case of the photodissociation of N_2O.[21] In fact, the signs of the multipole moments are also the same as those observed in the case of N_2O, although in the present case the $J = 1$ atoms are relatively unpolarized compared with their $J = 2$ counterparts.

4. Discussion

4.1. Orbital and Spin Polarization. In our previous work on the 193-nm photodissociation of N_2O, a simple model was developed to help interpret the O-atom alignment measurements.[21] It was assumed that the recoil of the O atom was sufficiently fast compared with the time scale of spin−orbit coupling[43] that in the exit channel the system evolved diabatically into products. Importantly, it was assumed, furthermore, that the O-atom electron spin was unpolarized. Although it might be true that in the exit channel of the photodissociation of SO_2 the relative motion of the photofragments is also fast, there are several reasons that the assumption of unpolarized electron spin in the present system might be invalid.

One can think of the photodissociation of SO_2 as occurring via two interconnected regions. Region 1 includes the Franck−Condon and close interaction regions, where the excited SO_2 molecule is trapped on a time scale of tens of picoseconds. This is likely to correspond to the wells on either the ground $1^1A'$ or excited $2^1A'$ potential energy surfaces. Region 2 corresponds to the exit channel region, where the fragments separate rapidly, in the present case with a relative velocity of around 2700 m s^{-1}. The boundary between regions 1 and 2 could, for example, be taken to be the crossing seam between the $2^1A'$ and the $2^3A'$ states or the avoided crossing between the $2^1A'$ and the $3^1A'$ states. The possible involvement of triplet states, either in region 1 or at the intersection between regions 1 and 2, means that it is unsafe to assume that the total electron spin of the parent molecule, S_{tot} ($\neq 0$), remains unpolarized. If the parent molecular spin were polarized on entering region 2 and the motion in region 2 were rapid compared with the time scale for spin−orbit coupling, then (as will be shown below) spin-polarized oxygen atoms would be generated. In this case, rapid motion in region 2 ensures that the spin polarization is unchanged from that established on entry into that region. A further complication is that, unlike the situation in N_2O where the N_2 cofragment is a closed-shell species, here the O-atom cofragment is an open-shell $SO(^3\Sigma^-)$ species. This adds considerable complexity to the exit channel of this system compared with that in N_2O, which will not be treated rigorously here.

To overcome some of the difficulties outlined above, instead of neglecting spin polarization, here we fit the O-atom polarization data explicitly allowing for the possibility of O-atom spin polarization. We assume that on entering region 2 the exchange/electrostatic interaction is large compared with the spin−orbit interaction either within or between each evolving photofragment. The spin of the SO fragment in the exit channel of region 2 is treated as a spectator, but the spin−orbit interaction in the recoiling O atom is incorporated explicitly. Within these assumptions, it is possible to relate the state multipoles of the O-atom total angular momentum J to those of its orbital L and spin S angular momenta. As shown in our previous study of the photodissociation of N_2O,[21] the atomic state multipoles in the L, S representation can be related to those in the J, J' representation. (See eqs A1 and A2 of ref 21.) Specializing to the case where coherences between different spin−orbit states of oxygen are not measured, such that J is equal to J', yields the following expression for the state multipole moments of J

$$\rho_{KQ}(J) = \sum_{K_1,K_2}(2J+1)[(2K_1+1)(2K_2+1)]^{1/2} \times \begin{Bmatrix} L & L & K_1 \\ S & S & K_2 \\ J & J & K \end{Bmatrix} \sum_{q_1,q_2} C^{KQ}_{K_1 q_1 K_2 q_2}\, \rho_{K_1 q_1}(L)\, \rho_{K_2 q_2}(S) \quad (10)$$

where $\rho_{K_1 q_1}(L)$ and $\rho_{K_2 q_2}(S)$ are the state multipoles describing the electronic orbital angular momentum L and spin angular momentum S, respectively. The $C^{KQ}_{K_1 q_1 K_2 q_2}$ are Clebsch−Gordan coefficients. Note that for the real moments $\rho_{K\,-\,q} = (-1)^q \rho_{Kq}$, with $\rho_{00}(L) = 1/\sqrt{(2L+1)}$ and $\rho_{00}(S) = 1/\sqrt{(2S+1)}$. Whereas in the fast-recoil model previously employed the electron spin is assumed to be unpolarized,[21] such that the only nonzero moment is $\rho_{00}(S)$, here we fit the moments of S and L given the moments of J for $J = 1$ and 2. Because we have used only linearly polarized pump and probe radiation in the present study, we have information only about the alignment moments of J

TABLE 4: Molecular Frame Multipole Moments of the Electronic Orbital and Spin Angular Momenta, $\rho_{KQ}(L/S)$, for the O(^{3}P) Products of 193-nm SO_2 Photolysis, Averaged over Scattering Angle[a]

	$\rho_{KQ}(L/S)$	$\rho_{KQ}(S/L)$
$\rho_{20}(\cdots)$	−0.12(1)	−0.15(1)
$\mathscr{R}[\rho_{21}(\cdots)]$	−0.007(4)	−0.001(2)
$\rho_{22}(\cdots)$	+0.12(2)	−0.14(2)

[a] Errors in the last decimal place are given in parentheses. Note that the analysis does not allow the assignment of the moments are associated with *L* and those associated with *S*.

TABLE 5: Molecular Frame Multipole Moments of the Electronic Orbital and Spin Angular Momenta Showing the Molecular Frame Multipole Moments, $\rho_{KQ}(L)$, for O(^{3}P$_1$) and O(^{3}P$_2$) Obtained, Assuming that the O-Atom Spin Is Unpolarized[21,a]

$\rho_{KQ}(L)$	O(^{3}P$_1$)	O(^{3}P$_2$)
$\rho_{20}(L)$	−0.14(4)	−0.26(4)
$\mathscr{R}[\rho_{21}(L)]$	−0.003(3)	−0.006(4)
$\rho_{22}(L)$	−0.013(6)	−0.015(10)

[a] The fact that the moments for $J = 1$ and 2 are not the same suggests that the use of this model is inappropriate in the present case. (See the text for discussion.)

(i.e., K is even). Although terms with odd moments in S and L (i.e., odd K_1 and K_2) could contribute to the alignment of J, such terms have been neglected in the present study, and only even terms in K_1 and K_2 have been retained. In principle, the measurement of the orientation of J would allow this approximation to be avoided and the odd moments of L and S to be determined explicitly.

With the above model, it is possible to determine the three moments $\rho_{20}(\cdots)$, $\mathscr{R}[\rho_{21}(\cdots)]$, and $\rho_{22}(\cdots)$ for the spin and orbital angular momenta, as shown in Table 4. Note that because $S = L = 1$ for O(^{3}P) it is not possible to determine which set of derived multipole moments is associated with S and which is associated with L. The analysis also yields predictions for the spin−orbit state populations, $N(J) = (2J + 1)^{1/2}\rho_{00}(J)$, which, because the polarization is small, turn out to be very close to the statistical limit, in good agreement with the experiment. The inability to assign the moments to either the spin or the orbital angular momentum leads to uncertainty about the sign of the $\rho_{22}(L)$ moment. By contrast, the values derived for moments $\rho_{20}(L/S)$ and $\mathscr{R}[\rho_{21}(L/S)]$ are quite similar, and thus the sign and magnitude of these moments of L and S are determined quite precisely. Note that the analysis suggests that the spin angular momentum is polarized. The negative signs of $\rho_{20}(L/S)$ and $\rho_{20}(S/L)$ indicate that both S and L are preferentially aligned perpendicular to the recoil axis. Furthermore, the opposite signs of the two multipole moments $\rho_{22}(L)$ and $\rho_{22}(S)$ indicate that L and S lie preferentially perpendicular to one another.

It is informative to compare the present results for the multipole moments of the orbital angular momentum L with those that would have been obtained with the fast recoil model when all of the $K_2 \neq 0$ moments of S are constrained to zero. The fast-recoil multipole moments are shown in Table 5. Although the results of the two treatments yield qualitatively similar L-state multipole moments, as seen by a comparison of the data in Tables 4 and 5, the data of Table 5 confirm that it is inappropriate to neglect the spin polarization of the O atom because the predicted moments differ significantly for $J = 1$ and 2.

The presence of spin-polarized atomic oxygen is intriguing and might arise from two possible sources. It could be taken as evidence for the participation of triplet states, either in region 1 or, more likely in the present case, in region 2. If we assume that in region 2 dissociation proceeds rapidly, such that the spin polarization is unchanged in the exit channel, then it is possible to express the state multipole moments of the parent molecular spin S_{tot} in terms of the measured O-atom spin-polarization moments $\rho_{KQ}(S)$. In fact, this can be done simply by taking the inverse of the state multipole expansion, eq 10, replacing J with S_{tot}, L with S, and S with S_{SO}, the spin of the SO cofragment, and adapting the resulting equation for $K_2 = q_2 = 0$ (equivalent to taking the partial trace of the density matrix to allow for the fact that the SO cofragment is unobserved). The resulting equation can be written (see Appendix 1) as

$$\rho_{KQ}(S) = (-1)^{S+S_{SO}+S_{tot}+K}(2S_{tot}+1)\begin{Bmatrix} S & S & K \\ S_{tot} & S_{tot} & S_{SO} \end{Bmatrix}\rho_{KQ}(S_{tot}) \quad (11)$$

Note that only state multipoles with the same K and Q values are connected with each other. Thus, the $\rho_{KQ}(S_{tot})$ moments can be determined directly from the known $\rho_{KQ}(S)$ moments. If we assume specifically that a triplet state is involved in the photodissociation (i.e., $S_{tot} = 1$) then we obtain

$$\rho_{2Q}(S) = -\frac{1}{2}\rho_{2Q}(S_{tot})$$

This would indicate that whereas the spin of the O-atom fragment lies preferentially perpendicular to the recoil direction the total spin is aligned along the recoil direction. The factor of $^1/_2$ reflects the fact that this model predicts that the two photofragments will have the same spin polarization.

Alternatively, spin polarization may arise from a breakdown of the fast recoil approximation in region 2. The O-atom spin−orbit coupling constant is $E_{SO} \approx 80$ cm^{-1}. The relative velocity of the fragments in the exit channel is ∼2700 m s^{-1}, yielding a relative kinetic energy of ∼3600 cm^{-1} (i.e., some 45 times the O-atom spin−orbit splitting). Although this number is large, the estimated time scale for spin−orbit coupling is $\hbar/E_{SO} \approx 60$ fs, in which time the fragments separate about 1.8 Å. This raises the possibility that the polarization of the O-atom spin occurs in the recoupling region and is not necessarily a result of dissociation along a triplet pathway. It is relevant to note that, in a study of the photodissociation of O_2 at 157 nm, Huang and Gordon found O(^{3}P) fragments formed mainly in $J = 2$ (i.e., adiabatic behavior), and the kinetic energy roughly twice that observed here.[47] They also computed a recoupling distance of about 1−2 Å, similar to that estimated here.

With a knowledge of the multipole moments of L, it is possible to determine the unpaired electron density of the recoiling O atoms.[21] In the case of two unpaired electrons residing in p orbitals, appropriate to the treatment of ground electronic state oxygen, the unpaired electron density may be written as[21]

$$N(\theta,\phi) = \frac{1}{2\pi}\left\{1 + \frac{3}{2\sqrt{6}}(3\cos^2\theta - 1)\rho_{20}(L) - 3\cos\theta\sin\theta\cos\phi\,\mathscr{R}[\rho_{21}(L)] + \frac{3}{2}\sin^2\theta\cos 2\phi\,\rho_{22}(L)\right\} \quad (12)$$

where we have used the fact that $\rho_{00}(L) = 1/\sqrt{3}$. Substituting either set of multipole moments in Table 4 yields an unpaired electron density function that peaks perpendicular to the molecular-frame z axis, defined as the O-atom recoil direction. The uncertainty in the moment $\rho_{22}(L)$, mentioned above,

manifests itself as uncertainty in whether the unpaired electron density peaks in the molecular-frame *zx* plane (i.e., that containing the recoil velocity and the electric vector of the photolysis radiation) or the *zy* plane. The negative sign of the $\rho_{20}(L)$ moment might be taken to suggest the assignment of the exit channel to a potential energy surface of Σ symmetry at linearity, as was inferred in our study of N_2O.[21] In the following section, we refine these arguments further by examining the angular dependence of the long-range region of the potentials correlating with $O(^3P) + SO(^3\Sigma^-)$ (or $N_2(^1\Sigma^+)$) separated products.

4.2. Long-Range Potentials and Predicted Orbital Polarization. Here we follow the procedure employed to model polarization effects in the singlet channel of the photodissociation of N_2O.[44] We define a critical separation, R_c, in region 2, at which point the electrostatic interaction is large compared with the spin−orbit coupling. Furthermore, we assume that

(i) before the critical separation R_c the system evolves adiabatically on some potential energy surface (the model does not say which one);

(ii) the electronic wave function at this critical point is determined by first-order electrostatic interactions;

(iii) after this point the fragments lose any contact and the wave function, transformed to the appropriate frame, determines the observed orbital angular momentum polarization of the oxygen atoms;

(iv) effects of the coherent excitation of two surfaces are ignored.

In this subsection, we take the molecular-frame *z* axis to lie along the Jacobi coordinate *R*, with the diatomic molecule lying in the *zx* plane. The long-range interaction potential energy matrix, $V_{MM'}$ can then be constructed in a basis $|\chi LM\rangle$, where $|\chi\rangle$ is the wave function for diatomic molecule A, and $|LM\rangle$ is the electronic orbital wave function for atom B. (Here we rewrite M_L as *M*.) Expressing the matrix $V_{MM'}$ in terms of a multipole expansion yields

$$\begin{aligned} V_{MM'}(\gamma) &= \langle \chi LM|\hat{V}(\gamma)|\chi LM'\rangle \\ &= \sum_{l_A,l_B} \frac{\langle \chi|\hat{Q}_{l_A0}|\chi\rangle\langle L||\hat{Q}^{(l_B)}||L\rangle}{R^{l_A+l_B+1}}(-1)^{l_A+L-M}\left[\frac{(2l_A+2l_B+1)!}{(2l_A)!(2l_B)!}\right]^{1/2} \\ &\times \sum_{m_A}\begin{pmatrix} l_A & l_B & l_A+l_B \\ m_A & -m_A & 0\end{pmatrix}\begin{pmatrix} L & l_B & L \\ -M & -m_A & M'\end{pmatrix} C_{l_Am_A}(\gamma,0) \end{aligned} \quad (13)$$

where $C_{l_Am_A}(\cdots)$ is a modified spherical harmonic and the terms in brackets are 3*J* symbols. $\langle \chi|\hat{Q}_{l_A0}|\chi\rangle$ is the expectation value of the multipole moment operator of diatomic molecule A, and $\langle L||\hat{Q}^{(l_B)}||L\rangle$ is the reduced matrix element of the multipole moment operator of atom B. (See below.) Diagonalization of the matrix, *V*, for a given value of γ, yields the eigenvalues (i.e. the long-range potential energy surfaces) and eigenfunctions (i.e., the electronic wave functions in the $|\chi LM\rangle$ basis). The latter are used to provide the multipole moments via the equation[45]

$$\rho_{KQ}(L) = \sum_{MM'}(-1)^{L-M}\langle LM, L-M'|KQ\rangle\rho_{MM'}(L)$$

with density matrix elements

$$\rho_{MM'}(L) = c^*_{M'}c_M = c_{M'}c_M$$

Here c_M are the (real) expansion coefficients of the wave function for the electronic state of interest. In the following discussion, we have assumed that the critical point R_c is at sufficiently large *R* that it can safely be taken to be the recoil direction. Hence, we have not transformed the $\rho_{MM'}(L)$ into the molecular frame used in the experiments, which is defined with *z* along the recoil direction. It should also be mentioned that the present calculation neglects the shift of the CM of the SO moiety, which is located here at the center of the bond.

In the case of SO_2, the SO photofragment possesses both a dipole and a quadrupole moment; therefore, the specific terms of interest in the above expansion are the quadrupole−quadrupole term, for which $l_A = l_B = 2$, and the dipole−quadrupole term, for which $l_A = 1$ and $l_B = 2$. These two terms give rise to $1/R^5$ and $1/R^4$ contributions to the long-range potential, respectively, as seen from eq 13. In the present work, we have not attempted to quantify matrix elements $\langle \chi|\hat{Q}_{l_A0}|\chi\rangle$ and $\langle L||\hat{Q}^{(l_B)}||L\rangle$, and thus at the (unknown) critical distance, the ratio of dipole and quadrupole moments is not known. (Note that for $N_2 + O(^3P/^1D)$ this complication does not arise[44] because N_2 does not possess a dipole moment.) We have therefore calculated both the quadrupole−quadrupole and quadrupole−dipole terms and show that similar conclusions can be drawn from a consideration of either. Of course, one would expect the quadrupole−dipole term to become increasingly dominant as *R* increases.

As discussed in the Introduction, at linearity the $O(^3P) + SO(^3\Sigma^-)$ products correlate with surfaces of $^{1,3,5}\Sigma^+$ and $^{1,3,5}\Pi$ symmetry. In common with previous studies, the possible involvement of the quintet surfaces is neglected here. For the singlet surfaces at Jacobi angles in the range of $0 \le \gamma \le 90°$, the $^1\Sigma^+(^1A')$ is the lowest in energy[6] and correlates with the ground electronic state of SO_2. The signs of the multipole terms in eq 13 are consistent with this energy ordering. The angular dependences of the potentials for the triplet states and the predicted state multipole moments, discussed below, are the same as those shown for the singlet states. Slices through the relevant potential energy surfaces as a function of γ, determined from the quadrupole−quadrupole and quadrupole−dipole terms in the expansion of eq 13, are shown in Figure 7. Both the dipole−quadrupole and quadrupole−quadrupole long-range interactions favor a preferred linear OSO configuration in the ground electronic state. The symmetry labels have been identified by considering the $|M|$ populations determined from the eigenfunctions as indicated above. (They are in fact the diagonal elements of the density matrix.) Note that for the quadrupole−dipole interaction the A″ electronic state (i.e., that with the both O-atom unpaired electrons in the molecular plane) the potential energy at $\gamma = 90°$ is identically zero, which it must be by symmetry in this case, because the CM of diatomic fragment A is located in the middle of the bond. Notice also the avoided crossing between the two states of A′ at $\gamma = 90°$.

The predicted multipole moments $\rho_{2Q}(L)$ are shown in Figure 8 versus Jacobi angle γ for the Σ and Π states under discussion. (The same plots apply to both the singlet and triplet states.) For the $\Pi(A'')$ state, the multipole moments predicted by both the quadrupole−quadrupole and quadrupole−dipole terms are independent of γ. This is physically reasonable because this state corresponds to that with the filled p orbital of the O atom out of the plane of the molecule. Note also that because this state is the only one of A″ symmetry there are no other states with which it can mix, and the moment $\mathcal{R}[\rho_{21}(L)]$ is zero. The behavior of the moments for the two A′ states is rather more complex because the orbital character of the states changes as γ varies from 0 to 180°. Thus, the ground state at 0° (i.e., for

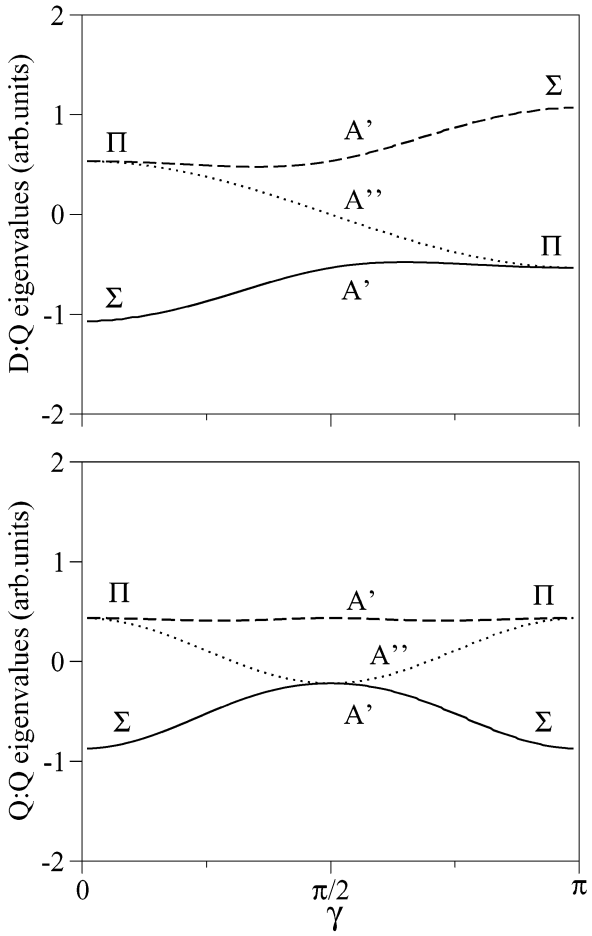

Figure 7. γ dependence of the quadrupole−dipole (upper panel) and quadrupole−quadrupole (lower panel) terms in the potential energy for the three singlet states generated upon the combination of SO($^3\Sigma$) and O(^{3}P).

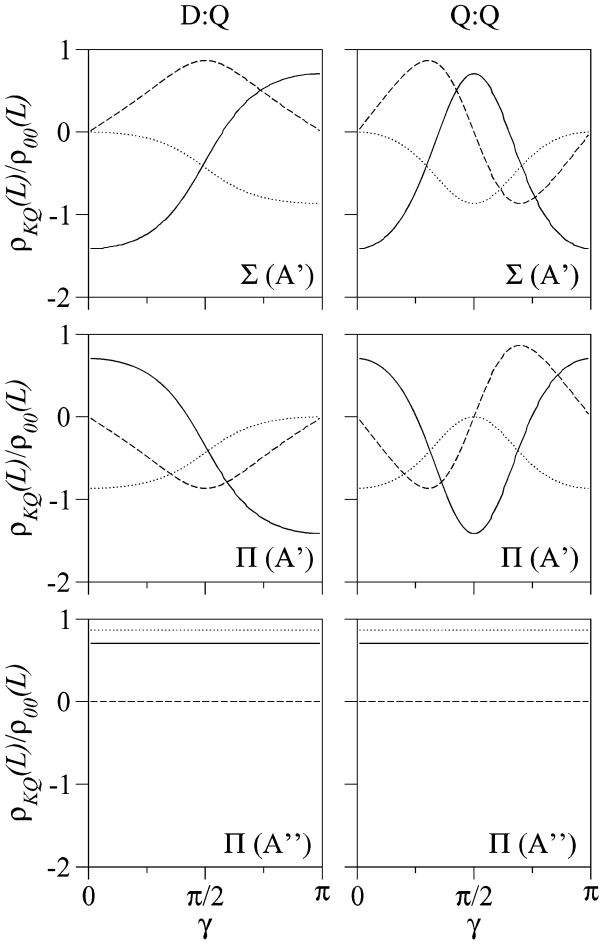

Figure 8. Predicted $\rho_{KQ}(L)$ versus Jacobi angle γ for the three singlet states under discussion, employing the quadrupole−dipole interaction term (left panels) and quadrupole−quadrupole interaction terms (right panels). — $\rho_{20}(L)$, − − − $\mathscr{R}[\rho_{21}(L)]$, and ··· $\rho_{22}(L)$.

OSO) is a Σ state, and $\rho_{20}(L) < 0$, corresponding to preferential population of the $M = 0$ sublevel of the O atom, whereas at $\gamma = 180°$ (i.e., for SOO) the ground state has Π symmetry and $\rho_{20}(L) > 0$, corresponding to preferential population of the $M = \pm 1$ sublevels. Because of the mixing between the two A′ states away from linearity, both of these states have nonzero values of $\mathscr{R}[\rho_{21}(L)]$.

4.3. Mechanistic Implications. The nuclear motion over the surfaces described in the previous subsection will lead to averaging over the γ coordinate. This averaging is probably one important reason that the predicted moments shown in Figure 8 are much larger than those observed experimentally. Correct averaging over this coordinate requires a full dynamical calculation, which if performed rigorously would also allow for nonadiabatic transitions induced, for example, via spin−orbit coupling. Such a complete treatment is not feasible at present and has not been performed. Nevertheless, the calculated multipole moments do provide some clues about the dissociation mechanism in the exit channel. Here we focus our discussion on the alternative singlet dissociation channels, although at present, on the basis of the alignment measurements alone, it is not possible to rule out the involvement of an intersystem-crossing mechanism. It would appear that the measured polarization parameters of Table 4 are inconsistent with dissociation on a surface of Π(A″) symmetry. The calculated moments are of the wrong sign and relative magnitude to be compatible with the experimental data. The fact that the predicted moments for this state are invariant with γ suggests that this picture would not change significantly if the photodissociation dynamics were considered more fully.

It is necessary, though, to be more cautious about assigning roles for the two A′ states. In the case of the singlet states of SO_2, these correlate with the ground 1^1A′ state and, at long range, the repulsive 2^1A′ state, whereas for the triplet states the Σ(A′) and Π(A′) states correlate with the 2^3A′ and 1^3A′, respectively. The predicted multipole moments for these states change sign at ∼90 and 45° for the quadrupole−dipole and quadrupole−quadrupole terms, respectively, and thus the dynamical averaging over the Jacobi angle is more critical. Both the ground and excited states of SO_2 have similar equilibrium bond angles, corresponding at long range to Jacobi angles of $\gamma \approx 60°$. The potential energy surfaces of Katagiri et al.[6] indicate that little torque is likely to be generated by dissociation proceeding via the ground-state surface, whereas dissociation on the excited singlet state surface via the avoided crossing with the 3^1A′ state would appear likely to generate more activity in the angular coordinate, favoring large γ. (Note that our definition of γ is different from that used by Katagiri et al.[6]) This singlet channel mechanism, which is that favored in the interpretation offered by Houston and co-workers,[11] might be consistent with the present alignment data but only if large Jacobi angles are preferentially sampled. It is perhaps worth commenting that such a mechanism might also be expected to generate significant photofragment rotational excitation, which is not observed either in the present study or in previous work.[11,37]

As noted above, an alternative mechanism, photodissociation proceeding via excitation to the C state, followed by internal conversion back to the ground state, would be expected to generate little rotational excitation in the SO coproduct. The predicted multipole moments for both types of interaction terms are consistent with this mechanism provided that the average γ sampled at the critical separation is similar to the equilibrium values in the parent states. This interpretation of the alignment data would seem to be more consistent with the modest SO photofragment rotational excitation observed both at 193 nm and in the range of 202−207 nm.[11] It is also consistent with the findings of the recent IR emission study from the group of Weiner and co-workers.[17] However, it is important to emphasize that from the *L*-state multipole moments alone it is not possible to distinguish between the internal-conversion mechanism and the intersystem-crossing mechanism, which proceeds via the $2^3A'$ state, because both states would be predicted to generate the same *L* polarization. The participation of the triplet state has been invoked previously to account for the presence of spin-polarized SO fragments.[4,8] Indeed, as discussed in section 4.1, the observation of spin-polarized oxygen might be taken as a signature of the involvement of the triplet state.

As a final comment, it is worthwhile to compare the calculated polarization information with that observed in the spin-forbidden dissociation channel of N_2O, which generates $O(^3P) + N_2(^1\Sigma^+)$ products. As noted above, in this system only the long-range quadrupole−quadrupole interaction need be considered. The angular dependence of the quadrupole−quadrupole interaction potential has the same form as that shown in the lower panel of Figure 7, although the ordering of the Π and Σ states in N_2O is reversed compared with that shown for SO_2 (i.e., the Σ state is highest in energy). Furthermore, the A′ and A″ symmetry labels used in Figures 7 and 8 should be exchanged for N_2O because the O-atom cofragment is $N_2(^1\Sigma^+)$, which transforms as A′ in C_s symmetry, as opposed to $SO(^3\Sigma^-)$ from SO_2, which transforms as A″. According to an analysis of the polarization data using the fast-recoil model, the photodissociation of N_2O generates O atoms with negative values for all of the $\rho_{2Q}(L)$ moments, with $\rho_{20}(L)$ taking a value of ~ -0.14. This was interpreted as arising from dissociation in the exit channel for a state of $^3\Sigma^-$(A″) symmetry. Although it is clear from the data shown in the right-hand panel of Figure 8 that the calculated multipole moments might be consistent with this picture, it is also clear that a more quantitative assignment requires some knowledge of the Jacobi angles sampled in the dissociation, preferably derived from a scattering calculation. Furthermore, given that photodissociation in N_2O is likely to involve intersystem crossing, it would also be of interest to examine whether the O-atom spin is polarized using the model described in the present work.

5. Conclusions

The 193-nm photodissociation of SO_2 has been studied using resonantly enhanced multiphoton ionization of ground-state $O(^3P)$, coupled with velocity-map ion imaging. The dependence of the ion images on the linear polarization of pump and probe laser radiation has been used to determine the electronic angular momentum alignment of the $O(^3P_J)$ atoms, together with their speed distribution and translational anisotropy. The data are interpreted with the help of a model that accommodates the polarization of the O-atom electron spin. The analysis suggests that both the O-atom electron spin and orbital angular momenta are polarized perpendicular to the recoil direction. The angular dependence of the long-range quadrupole−dipole and quadrupole−quadrupole potential energy terms in the exit channel is also considered, from which molecular-frame multipole moments of the recoiling O atoms have been estimated. The predicted multipole alignment moments are shown to depend sensitively on the Jacobi angle, γ, suggesting that a more quantitative assessment of polarization effects in this and similar systems requires a dynamical treatment that takes into account the averaging over this angular coordinate. Nevertheless, it has been shown that a comparison of the calculated polarization moments with those derived experimentally can been used even at a qualitative level to discount some of the possible dissociation pathways. The calculations also lend some support to the mechanism proposed previously for the spin-forbidden photodissociation of N_2O leading to $O(^3P) + N_2$ products,[21] although the Jacobi angle is also seen here as crucial in determining the values of the polarization parameters.

Acknowledgment. The Oxford group thanks the Royal Society and the EPSRC for research grants. We also gratefully acknowledge the EU (through project number HPRN-CT-1999-00007) for their support of a Research Training Network. O.S.V gratefully acknowledges a grant from the Russian Foundation for Basic Researches N 02-03-32914.

Appendix 1

The relationship between atomic-state multipoles ρ_{KQ} in the J_1, J_2, and J, J' representations can be written as

$$[\rho_{K_1}(J_1) \otimes \rho_{K_2}(J_2)]_{KQ} = \sum_{J,J'} [(2J+1)(2J'+1)(2K_1+1)(2K_2+1)]^{1/2} \times \begin{Bmatrix} J_1 & J_1 & K_1 \\ J_2 & J_2 & K_2 \\ J & J' & K \end{Bmatrix} \rho_{KQ}(J, J') \quad (14)$$

which is the inverse of eq A1 in ref 21. Here $\rho_{KQ}(J, J')$, with rank *K*, is the state multipole related to the total angular momenta *J*, *J′*, and $\rho_{K_1}(J_1)$ and $\rho_{K_2}(J_2)$, with their ranks K_1 and K_2, are the state multipoles related to angular momenta J_1 and J_2, respectively. The direct tensor product in eq 14 is readily calculated according to the equation

$$[\rho_{K_1}(J_1) \otimes \rho_{K_2}(J_2)]_{KQ} = \sum_{q_1,q_2} C^{KQ}_{K_1 q_1 K_2 q_2} \rho_{K_1 q_1}(J_1)\, \rho_{K_2 q_2}(J_2) \quad (15)$$

where $C^{KQ}_{K_1 q_1 K_2 q_2}$ is a Clebsch−Gordan coefficient.

Because in the present application fragment 2 is unobserved, we take the partial trace over J_2 in eq 14, which is equivalent to holding $K_2 = 0$. Then, $K_2 = 0$, $q_2 = 0$, and eq 15 simplifies to

$$[\rho_{K_1}(J_1) \otimes \rho_{K_2}(J_2)]_{KQ} = \delta_{K,K_1} \delta_{Q,q_1} \delta_{K_2,0}\, \rho_{KQ}(J_1)\, \rho_{00}(J_2) \quad (16)$$

and the 9*j* symbol in eq 14 collapses to

$$\begin{Bmatrix} J_1 & J_1 & K_1 \\ J_2 & J_2 & 0 \\ J & J' & K \end{Bmatrix} = \delta_{K,K_1} \frac{(-1)^{J_1+J'+K+J_2}}{[(2K+1)(2J_2+1)]^{1/2}} \begin{Bmatrix} J_1 & J_1 & K \\ J & J' & J_2 \end{Bmatrix} \quad (17)$$

In the case of coupling the two spins $J_1 = S$ and $J_2 = S_{SO}$ into the total spin S_{tot} (using the notation of section 4.1), which we consider to have definite values of either $S_{tot} = S'_{tot} = 0$ or

$S_{tot} = S'_{tot} = 1$, no summation over S_{tot} is necessary in eq 14. By combining these results, eq 14 can be written as

$$\rho_{KQ}(S)\,\rho_{00}(S_{SO}) = (-1)^{S+S_{SO}+S_{tot}+K}\frac{(2S_{tot}+1)}{\sqrt{2S_{SO}+1}}\begin{Bmatrix} S & S & K \\ S_{tot} & S_{tot} & S_{SO}\end{Bmatrix}\rho_{KQ}(S_{tot}) \quad (18)$$

Here $\rho_{00}(S_{tot}) = 1/\sqrt{2S_{tot}+1}$ by definition as a primary value, and the normalization factors for $\rho_{00}(S)$ and $\rho_{00}(S_{SO})$ are defined by eq 18. By considering the case for $K = 0$, it can be shown that $\rho_{00}(S) = 1/\sqrt{2S+1}$ and $\rho_{00}(S_{SO}) = 1/\sqrt{2S_{SO}+1}$. Substituting these expressions into eq 18 yields eq 11 of section 4.1.

Appendix 2

The multipole expansion of the Coulomb interaction between the diatomic molecule (A) and the atom (B) is given by[48]

$$\hat{V} = \sum_{l_A,l_B} R^{-(l_A+l_B+1)} \sum_{m_A,m_B} (-1)^{l_B}\left[\frac{(2l_A+2l_B)!}{(2l_A)!(2l_B)!}\right]^{1/2} \langle l_A m_A l_B m_B|(l_A+l_B)0\rangle \hat{Q}^{MF}_{l_A,m_A}\,\hat{Q}^{MF}_{l_B,m_B} \quad (19)$$

where the multipole operators ($\hat{Q}^{MF}$) are defined in the molecular frame. (See section 4.2.) In this Appendix, we derive the expression for the matrix elements of $\hat{V}$ in the $|\chi LM\rangle$ basis as given in eq 12. The computation of the diatomic part involves a rotation to the diatomic frame

$$\langle\chi|\hat{Q}^{MF}_{l_A,m_A}|\chi\rangle = \sum_{m'}\langle\chi|\hat{Q}_{l_A,m'}|\chi\rangle D^{l_A*}_{m_A,m'}(0,\gamma,0) \quad (20)$$

where $D^{l_A*}_{m_A,m'}(0,\gamma,0)$ is a Wigner rotation matrix element. Because the diatom is in a Σ^- state, only the term with $m' = 0$ contributes, and we may use $D^{l_A*}_{m_A,0}(0,\gamma,0) = C_{l_A,\,m_A}(\gamma,0)$. To evaluate the atomic part of the matrix elements, we use the Wigner−Eckart theorem:

$$\langle LM|\hat{Q}^{MF}_{l_B,m_B}|LM'\rangle = (-1)^{L-M}\begin{pmatrix} L & l_B & L \\ -M & m_B & M\end{pmatrix}\langle L||\hat{Q}^{(l_B)}||L\rangle \quad (21)$$

Finally, the expression for the matrix elements in eq 13 is obtained by converting the Clebsch−Gordan coefficient from eq 19 into a 3j symbol through

$$\langle l_A m_A l_B m_B|(l_A+l_B)0\rangle = \delta_{m_A,-m_B}(-1)^{l_A-l_B}(2l_A+2l_B+1)^{1/2}\begin{pmatrix} l_A & l_B & l_A+l_B \\ m_A & -m_A & 0\end{pmatrix} \quad (22)$$

References and Notes

(1) Okabe, H. *J. Am. Chem. Soc.* **1971**, *93*, 7095.
(2) Hui, M.-H.; Rice, S. A. *Chem. Phys. Lett.* **1972**, *17*, 474.
(3) Ivanco, M.; Hager, J.; Sharfin, W.; Wallace, S. C. *J. Chem. Phys.* **1983**, *78*, 6531.
(4) Ebata, T.; Nakazawa, O.; Ito, M. *Chem. Phys. Lett.* **1988**, *143*, 31.
(5) Becker, S.; Braatz, C.; Lindner, J.; Tiemann, E. *Chem. Phys.* **1995**, *196*, 275.
(6) Katagiri, H.; Sako, T.; Hishikawa, A.; Yazaki, T.; Onda, K.; Yamanouchi, K.; Yoshino K. *J. Mol. Struct.* **1997**, *413−414*, 589.
(7) Okazaki, A.; Ebata, T.; Mikami, N. *J. Chem. Phys.* **1997** *107*, 8752.
(8) Kanamori, H.; Butler, J. E.; Kawaguchi, K.; Yamada, C.; Hirota E. *J. Chem. Phys.* **1985**, *83*, 611.
(9) Tzyy-Schiuan, Y.; Myers, A. B. *J. Chem. Phys.* **1991** *95*, 6207.
(10) Ray, P. C.; Arendt, M. F.; Butler, L. J. *J. Chem. Phys.* **1998**, *109*, 5221.
(11) Cosofret, B. R.; Dylewski, S. M.; Houston, P. L. *J. Phys. Chem. A* **2000**, *104*, 10240.
(12) Bludský, O.; Nachtigall, P.; Hrusák, J.; Jensen P. *Chem. Phys. Lett.* **2000**, *318*, 607.
(13) Xie, D.; Guo, H.; Bludský, O.; Nachtigall, P. *Chem. Phys. Lett.* **2000**, *329*, 503.
(14) Chen, X.; Asmar, F.; Wang, H.; Weiner B. *J. Phys. Chem.* **1991**, *95*, 6415.
(15) Felder, P.; Effenhauser, C. S.; Huber, J. R.; *Chem. Phys. Lett.* **1988**, *148*, 417.
(16) Kawasaki, M.; Sato, H. *Chem. Phys. Lett.* **1987**, *139*, 585.
(17) Gong, Y.; Makarov, V.; Weiner, B. R. *Chem. Phys. Lett.* **2003**, *378*, 493.
(18) van Vroonhoven, M. C. G. N.; Groenenboom, G. C. *J. Chem. Phys.* **2002**, *116*, 1965.
(19) Bass, M. J.; Brouard, M.; Clark, A. P.; Vallance, C. *J. Chem. Phys.* **2002**, *117*, 8723.
(20) Bass, M. J.; Brouard, M.; Clark, A. P.; Martınez-Haya, B.; Vallance, C. *Phys. Chem. Chem. Phys.* **2003**, *5*, 856.
(21) Brouard, M.; Clark A. P.; Vallance, C.; Vasyutinskii, O. S. *J. Chem. Phys.* **2003**, *119*, 771.
(22) Bass, M. J.; Brouard, M.; Vallance, C.; Kitsopoulos, T. N.; Samartzis, P. C.; Toomes, R. L. *J. Chem. Phys.* **2003**, *119*, 7168.
(23) Martınez-Haya, B.; Bass, M. J.; Brouard, M.; Vallance, C.; Torres, I.; Barr, J. *J. Chem. Phys.*, in press.
(24) Chang, B. Y.; Hoetzlein, R. C.; Mueller, J. A.; Geiser, J. D.; Houston, P. L. *Rev. Sci. Instrum.* **1998**, *69*, 1665.
(25) Dixon, R. N. *J. Chem. Phys.* **1986**, *85*, 1866.
(26) Hertel, I. V.; Stoll, W. *Adv. At. Mol. Phys.* **1978**, *13*, 113.
(27) Bracker, A. S.; Wouters, E. R.; Suits, A. G.; Vasyutinski, O. S. *J. Chem. Phys.* **1999**, *110*, 6749.
(28) Rakitzis, T. P.; Kandel, S. A.; Alexander, A. J.; Kim, Z. H.; Zare, R. N. *J. Chem. Phys.* **1999**, *110*, 3351.
(29) Rakitzis, T. P.; Zare, R. N. *J. Chem. Phys.* **1999**, *110*, 3341.
(30) Mo, Y.; Suzuki, T. *J. Chem. Phys.* **1998** *109*, 4691.
(31) Kummel, A. C.; Sitz, G. O.; Zare, R. N. *J. Chem. Phys.* **1986**, *85*, 6874.
(32) Chang, B. Y.; Hoetzlein, R. C.; Mueller, J. A.; Geiser, J. D.; Houston, P. L. *Rev. Sci. Instrum.* **1998**, *69*, 1665.
(33) Abe, M.; Sato, Y.; Inagaki, Y.; Matsumi, Y.; Kawasaki, M. *J. Chem. Phys.* **1994**, *101*, 5647.
(34) Huang, Y. L.; Gordon, R. J. *J. Chem. Phys.* **1990**, *93*, 868.
(35) Becker, S.; Braatz, C.; Lindner, J.; Tiemann, E. *Chem. Phys. Lett.* **1993**, *208*, 15.
(36) Braatz, C.; Tiemann, E. *Chem. Phys.* **1998**, *229*, 93.
(37) Felder, P.; Haas, B.-M.; Huber, J. R. *Chem. Phys. Lett.* **1993**, *204*, 248.
(38) Yang, S.-C.; Bersohn, R. *J. Chem. Phys.* **1974**, *61*, 4400.
(39) Kawasaki, M.; Kasatani, K.; Sato, H.; Shinohara, H.; Nishi, N. *Chem. Phys.* **1982**, *73*, 377.
(40) Picheyev, B. V.; Smolin, A. G.; Vasyutinskii, O. S. *J. Phys. Chem. A* **1997**, *101*, 7614.
(41) Hall, G. E.; Houston, P. L. *Annu. Rev. Phys. Chem.* **1989**, *40*, 375.
(42) Simons, J. P. *J. Phys. Chem.* **1987**, *91*, 5378.
(43) Massey, H. S. W. *Rep. Prog. Phys.* **1949**, **12**, 248.
(44) Teule, J. M.; Groenenboom, G. C.; Neyer, D. W.; Chandler, D. W.; Janssen, M. H. M. *Chem. Phys. Lett.* **2000**, *320*, 177.
(45) Zare, R. N. *Angular Momentum: Understanding Spatial Aspects in Chemistry and Physics*; Wiley & Sons: New York, 1988.
(46) Hoy, A. R.; Brand, J. C. D. *Mol. Phys.* **1978**, *36*, 1409.
(47) Huang, Y. L.; Gordon, R. J. *J. Chem. Phys.* **1991**, *94*, 2640.
(48) van der Avoird, A.; Wormer, P. E. S.; Mulder, F.; Berns, R. M. *Top. Curr. Chem.* **1980**, *93*, 1.